Correspondence and requests for materials should be addressed to W.X.L. (wl240@ uowmail.edu.au) or Z.Q.S. (ziqi@ uow.edu.au)

Uncoupled surface spin induced exchange bias in α-MnO₂ nanowires

Wenxian Li[1,2], Rong Zeng[2], Ziqi Sun[2], Dongliang Tian[2,3] & Shixue Dou[2]

[1]School of Materials Science and Engineering, Shanghai University, Shanghai 200072, PR China, [2]Institute for Superconducting and Electronic Materials, University of Wollongong, NSW 2522, Australia, [3]Key Laboratory of Bio-Inspired Smart Interfacial Science and Technology of Ministry of Education, School of Chemistry and Environment, Beihang University, Beijing, PR China.

We have studied the microstructure, surface states, valence fluctuations, magnetic properties, and exchange bias effect in MnO₂ nanowires. High purity α-MnO₂ rectangular nanowires were synthesized by a facile hydrothermal method with microwave-assisted procedures. The microstructure analysis indicates that the nanowires grow in the [0 0 1] direction with the (2 1 0) plane as the surface. Mn³⁺ and Mn²⁺ ions are not found in the system by X-ray photoelectron spectroscopy. The effective magnetic moment of the manganese ions fits in with the theoretical and experimental values of Mn⁴⁺ very well. The uncoupled spins in $3d^3$ orbitals of the Mn⁴⁺ ions in MnO₆ octahedra on the rough surface are responsible for the net magnetic moment. Spin glass behavior is observed through magnetic measurements. Furthermore, the exchange bias effect is observed for the first time in pure α-MnO₂ phase due to the coupling of the surface spin glass with the antiferromagnetic α-MnO₂ matrix. These α-MnO₂ nanowires, with a spin-glass-like behavior and with an exchange bias effect excited by the uncoupled surface spins, should therefore inspire further study concerning the origin, theory, and applicability of surface structure induced magnetism in nanostructures.

N anostructures have received steadily growing interest as a result of their peculiar and fascinating properties and their superiority to their bulk counterparts. The strongly size-related properties of nanomaterials offer unexpected and unprecedented behaviours, which bears great potential for innovative technological applications[1–5]. Magnetic nano materials have attracted intensive research interest among magnetism researchers for decades due to their huge potential in technological applications, both in magnetic applications such as recording technology and in multidisciplinary exploration such as biology and medicine[6–9]. The large specific surface area induces novel magnetic behaviour, such as exchange bias in pure ferromagnetic, ferrimagnetic, and antiferromagnetic nanoparticles[10]. Exchange biasing has important technological applications. Powdered exchange biased nano materials have found practicle applications in magnetic recording media[11]. Exchange biased core–shell, ferromagnetic−antiferromagnetic (FM–AFM), nanoparticles have been proposed as possible flux amplifiers for magnetic resonance settings, such as in magnetic resonance imaging[12]. A practicle application of exchange bias in nano materials has been proposed theoretically for stabilizing the magnetization of nanostructures against thermal fluctuations[13]. The development of "spintronics" devices with higher spin degree of freedom shows the advantage of higher speeds, non-volatility, and reduced power consumption[14,15]. The exchange biased nanostructures play a critical role in the main exponents of the spin based electronics, i.e., spin valves and magnetic tunnel junctions[16].

The finite-size effect refers to the significance of the surface spin induced ferromagnetism (FM) in nano materials consisting of an antiferromagnetic (AFM) material as the size decreases[17,18]. Antiferromagnet usually has two mutually compensating sublattices and the asymmetrical surface atom/ion distribution always breaks the sublattice pairing and thus leads to "uncompensated" surface spins. This effect was initially discussed by Néel to explain the origination of net magnetic moment in AFM nanoparticles[19]. The existence of exchange bias properties in pure nanoparticles can be determined through the observation of hysteresis loop shifts along the field axis after field cooling. Several experimental studies indicate various scenarios responding for the magnetic properties, such as spin-glass or cluster-glass-like behaviour of the surface spins[20,21], thermal excitation of spin-precession modes[22], finite-size induced multisublattice ordering[23], core-shell interactions[20,21], or weak ferromagnetism[24,25]. Surface spin canting and surface spin disorder were confirmed by inelastic neutron scattering[26], Mössbauer spectroscopy[27], X-ray absorption and dichroism[28], and polarized neutron diffraction[29].

In this work, we synthesized AFM α-MnO₂ nanowires with the help of microwave radiation to investigate the surface spin contributions in AFM nanosystems. We have focused on the exchange-bias properties and the origin of ferromagnetism by employing systematic magnetic measurements and analysis. We have found and confirmed

1

two important sources of magnetic contributions in the nanostructures: (i) regular antiferromagnetically ordered nanostructure cores, and (ii) uncoupled surface spins, which contribute to the magnetic moments and present spin-glass-like magnetic behaviour. It should be noted that there are no detectable Mn^{3+} and Mn^{2+} ions in our sample and that exchange bias has been found in high purity α-MnO_2 for the first time.

Results

Microstructure, phase, and valence state. Images of the microstructure observed by scanning electron microscopy (SEM), as shown in Figure 1(a), and transmission electron microscopy (TEM), as shown in Figure 1(b), make it clear that the α-MnO_2 presents as nanowires with a diameter of 20 nm and a length of 1 μm. The high resolution TEM (HRTEM) image and the selected area electron diffraction (SAED) pattern shown in Figure 1(d) indicate that the α-MnO_2 nanowires grow in the [0 0 1] direction and that the rough surface (Figure 1(c)) is parallel to the (2 1 0) plane.

Our sample is high purity α-MnO_2 as indicated by the X-ray diffraction (XRD) pattern shown in Figure 2(a). All peaks were indexed by α-MnO_2. α-MnO_2 has a tetragonal Hollandite-type structure with the space group $I4/m$, in which the MnO_6 octahedra are linked to form double zigzag chains along the c-axis by edge-sharing. These double chains then share their corners with each other forming approximately square tunnels parallel to the c-axis, as shown in the inset of Figure 2(a). The refined lattice constants are $a = b = 0.9865$ nm and $c = 0.2897$ nm. Compared with the theoretical lattice parameters of α-MnO_2, the lattice of α-MnO_2 nanowires is expanded due to the high density of defects in the nanostructures. The large lattice parameters can be easy deduced from the shifted diffraction peaks shown in Figure 2(a), especially the (h k 0) planes. Furthermore, the (2 1 1) peak of the sample is obviously higher than the peak in the standard polycrystalline diffraction (ICSD 44–141). This confirmed the conclusion deduced from the SAED pattern.

The valence state of Mn is very flexible from 0 to +7 because of its valence shell configuration of $3d^5 4s^2$. Mixed valences have been found in MnO_x[30], $MnO(OH)$[31], and $CaMnO_3$[32]. For the MnO_2 with nanowire structure in this work, the phase has been confirmed as high purity α-MnO_2 by XRD. The surface sensitive X-ray photoelectron spectroscopy (XPS) technique was employed to examine the valence state of α-MnO_2 nanowires. The high resolution scans of $2P_{1/2}$ and $2P_{3/2}$ were fitted with four Gaussian-Lorentz peaks, p1–p4, respectively, as shown in Figure 2(b). p1 and p2 are responsible for the observed $2P_{1/2}$ peak of Mn^{4+}, and p3 and p4 for the $2P_{3/2}$. The binding energies of p1 and p3 are 653.75 and 642.26 eV, which are in good agreement with $2P_{1/2}$ and $2P_{3/2}$ of Mn^{4+}. The binding energies of p2 and p4 are 654.85 and 643.60 eV, which are also attributed to $2P_{1/2}$ and $2P_{3/2}$ of Mn^{4+}. The peak splitting of $2P_{1/2}$ and $2P_{3/2}$ comes from the coupling of angular momenta associated with partially filled core and valence shells containing unpaired electrons of Mn^{4+} [33,34]. The two different states are present in the ratio of $\sim$1.4 : 1. The Mn^{3+} and Mn^{2+} contributions to the XPS are always shown as a small shoulder on the low energy side of p3 in the region of the circle in Figure 2(b). However, this phenomenon is absent in our sample, which means that only Mn^{4+} ions exist in our sample. At least, the Mn^{2+} and Mn^{3+} contents are below the detection limit of XPS.

Magnetization. MnO_2 has been reported as an antiferromagentic material with a Néel temperature (T_N) of $\sim$24.5 K[35]. The magnetization dependence on temperature ($M(T)$) is shown in Figure 3. Both zero field cooling (ZFC) effects and field cooling (FC) effects were measured under 100 Oe magnetic field. The magnetic moment increased with decreasing temperature in both cases. The magnetic moment is significantly enhanced below about 100 K, which can be confirmed by the deviation from linear behaviour of the $1/M(T)$ vs. T curve, demonstrating the tendency towards ferromagnetism at low temperature. The ferromagnetic behavior at low temperature is confirmed by the hysteresis loop shape in the field dependent magnetization, as shown in Figure 4(a). In addition, the ZFC magnetization curve bifurcates from the FC one below $\sim$50 K, as indicated by the dM/dT vs. T curves, and shows a peak at $\sim$13 K, which is an indication of glassy behavior at low temperature[36]. The $M(T)$ behaviour is in agreement with the temperature dependence of the magnetic susceptibility expected for polycrystalline antiferromagnetic materials with T_N of 13 K. The T_N value is compatible with $T_N = 13$ K for α-MnO_2 nanowires[37], but is much lower than 24.5 K of α-MnO_2 single crystal[35]. The lower T_N values of nanosized α-MnO_2 can be attributed the small size effect as demostrated in ferromagnetic $Fe_{83}Nd_{13}B_4$ by Mulyukov et al.[38]. It should be noted that the magnetic moment in the high temperature region on the FC curve is lower than on the ZFC curve because of the quick relaxation effect, which also influences the hysteresis loops.

The ground-state configuration of Mn^{4+} is $1s^2 2s^2 2p^6 3s^2 3p^6 3d^3$ with the excited state of $4F_{3/2}$, and its theoretical magnetic moment is 3.873 μ_B, with μ_B the Bohr magneton. The high temperature susceptibility data for α-MnO_2 was in good agreement with the Curie–Weiss law and therefore can be fitted to the following equation:

$$1/\chi = \frac{T - \theta}{C}, \qquad (1)$$

where $\chi = M(T)$, θ is the Curie–Weiss temperature, and C is the Curie–Weiss constant. The fitting result is indicated by the dashed-dotted line in Figure 3 with $\theta = -166$ K and $C = 1.816$. The negative θ value indicates the strong antiferromagnetic behaviour of the α-MnO_2 nanowires. The effective magnetic moment, μ_{eff}, is estimated from the Curie–Weiss constant based on the following equation:

$$\mu_{eff}^2 = \frac{3k_B C}{N_A \mu_B^2}, \qquad (2)$$

where k_B is the Boltzmann's constant and N_A Avogadro's constant. The Mn^{4+} in α-MnO_2 nanowires shows $\mu_{eff} = 3.811$ μ_B, which is a little lower than the theoretical value of 3.873 μ_B, but exactly the same
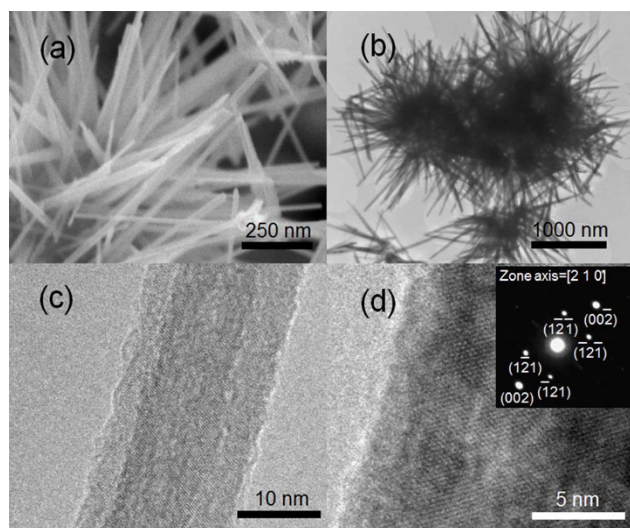

Figure 1 | Microstructural observation results for α-MnO_2 nanowires. (a), SEM image, (b), TEM image, (c), rough surface under TEM, and (d), HRTEM image of a single nanowire with inset SAED pattern. The images of the microstructure indicate that α-MnO_2 nanowires grow in the [0 0 1] direction, and the rough surfaces are parallel to the (2 1 0) planes. The diameter of the nanowires is $\sim$20 nm and the length $\sim$1 μm.
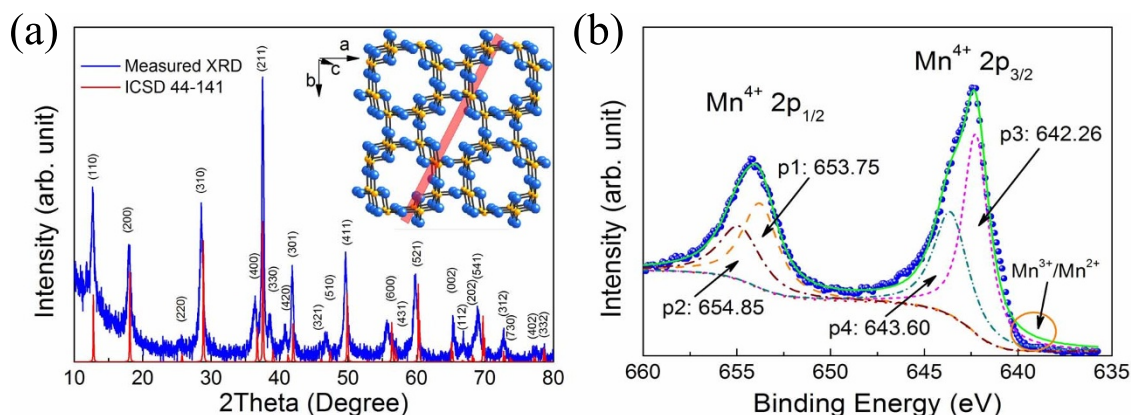
Figure 2 | **XRD pattern and X-ray photoelectron spectroscopy of α-MnO$_2$ nanowires.** (a), XRD pattern indexed as α-MnO$_2$ with lattice parameters of $a = b = 0.9865$ nm and $c = 0.2897$ nm. The inset shows the square tunnel structure of α-MnO$_2$ with the space group $I4/m$. The (210) plane is highlighted by the red shaded area. (b), X-ray photoelectron spectroscopy of α-MnO$_2$ nanowires. Fitted peaks p1 and p2 are responsible for the observed $2P_{1/2}$ peak of Mn^{4+}, and fitted peaks p2 and p4 for the $2P_{3/2}$. The peak splitting of $2P_{1/2}$ and $2P_{3/2}$ comes from the coupling of angular momenta associated with partially filled core and valence shells containing unpaired electrons of Mn^{4+} [33,34]. The orange circle indicates the possible positions of $2P_{3/2}$ for Mn^{3+} and Mn^{2+}.

as Mn^{4+} in CaMnO$_3$[32]. This is another evidence that only Mn^{4+} ions exist in the α-MnO$_2$ nanowires in this work.

Exchange Bias and Training Effect. The hysteresis loop at 5 K was measured after FC under 10 kOe, as shown in Figure 4(a). Although the whole loop shows antiferromagnetic behaviour due to the linear dependence of the magnetization moment on applied magnetic field, an obvious exchange bias was observed. This means that ferromagnetic clusters were formed on the surface of the nanowire structure. The magnitude of the exchange bias effect is usually compared quantitatively using the following two fields, the exchange-bias field H_{EB} and the coercive field H_c, defined, respectively, as

$$H_c = |H_{c1} - H_{c2}|/2 \text{ and} \tag{3}$$

$$H_{EB} = (H_{c1} + H_{c2})/2, \tag{4}$$

where H_{c1} and H_{c2} are the left and right coercive fields, respectively. H_{c1}, H_{c2}, H_c, and H_{EB} are -606, -306, 150, and 456 Oe, as
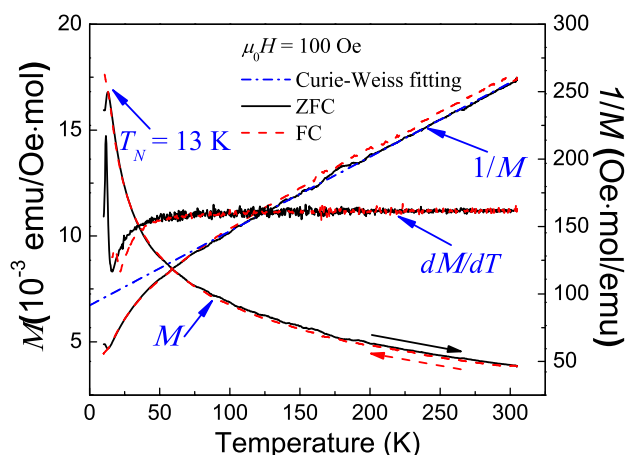

Figure 3 | **Magnetic behavior of α-MnO$_2$ nanowires.** $M(T)$ *vs.* T, $1/M(T)$ *vs.* T, $dM(T)/dT$ *vs.* T curves after zero field cooling (ZFC) and after field cooling (FC). The ZFC $1/M(T)$ *vs.* T curve is fitted with the Curie-Weiss law: $1/\chi = (T-\theta)/C$, using $\theta = -166$ K and $C = 1.816$, as indicated by the dot-dashed line.

indicated in upper inset of Figure 4(a). Another phenomenon is the open loop, as shown in lower inset of Figure 4(a), which was also observed in core-shell Co$_3$O$_4$ nanowires[39]. The magnetization moment depends greatly on the induced magnetic field because of the various surface states on the nanoparticles. The magnetization relaxation is the phenomenological origin of the training effect, as discussed below.

One of the most important properties of exchange biased systems is the existence of a so-called training effect. The performance of training effect is the reduction of H_{EB} and H_c in consecutive hysteresis loops at a fixed measurement temperature: H_{EB}(1st loop) $>$ H_{EB}(2nd loop) $> \cdots > H_{EB}$(n^{th} loop). The training effect can be explained in two steps: one the first reduction between the first and second loop and another one involving subsequent higher numbers of loops[40]. The first step of training effect was proposed to arise from the AFM magnetic symmetry[41]. The second step of training effect was demonstrated experimentally that the dependence of the H_{EB} reduction is proportional to the number of loops:

$$\mu_0 H_{EB}(n) - \mu_0 H_{EB}^e = \frac{\kappa}{\sqrt{n}} \text{ (for } n \geq 2), \tag{5}$$

where n is the number of loops traversed, κ is a system dependent constant, and $\mu_0 H_{EB}^e$ is the exchange bias field in the limit of infinite loops[42]. Based on this result, this second type of training effect is attributed to the reconfiguration of the AFM moments or domains during the continuous magnetization cycling[43]. The training effect in α-MnO$_2$ nanowires is in agreement with the second scenario described above, judging from the narrowing distance between the magnetization and demagnetization curves, as shown in the inset of Figure 4(b). Both H_c and H_{EB} decrease with the number of loops, as shown in Figure 4(b). The H_{EB} *vs.* n curve was fitted using Eq. (5) with $\kappa = -180$ Oe and $\mu_0 H_{EB}^e = -253$ Oe, as indicated by the dashed line in Figure 4(b). Eq. (5) fits the experimental data very well, and the result of the fit is extrapolated down to $n = 1$ in order to indicate the breakdown of the power-law behaviour at $n = 1$. The experimental data were also fitted using Eq. (5) from $n = 1$, as indicated by the dashed-dotted line in Figure 4(b). The fitting line deviates greatly from the experimental data, which indicates that the magnetization relaxes much more quickly from the first loop to the second loop than between the higher loops.

Although the power-law decay of the exchange bias has widely been observed, its origination still remains unexplained. Furthermore, Eq.
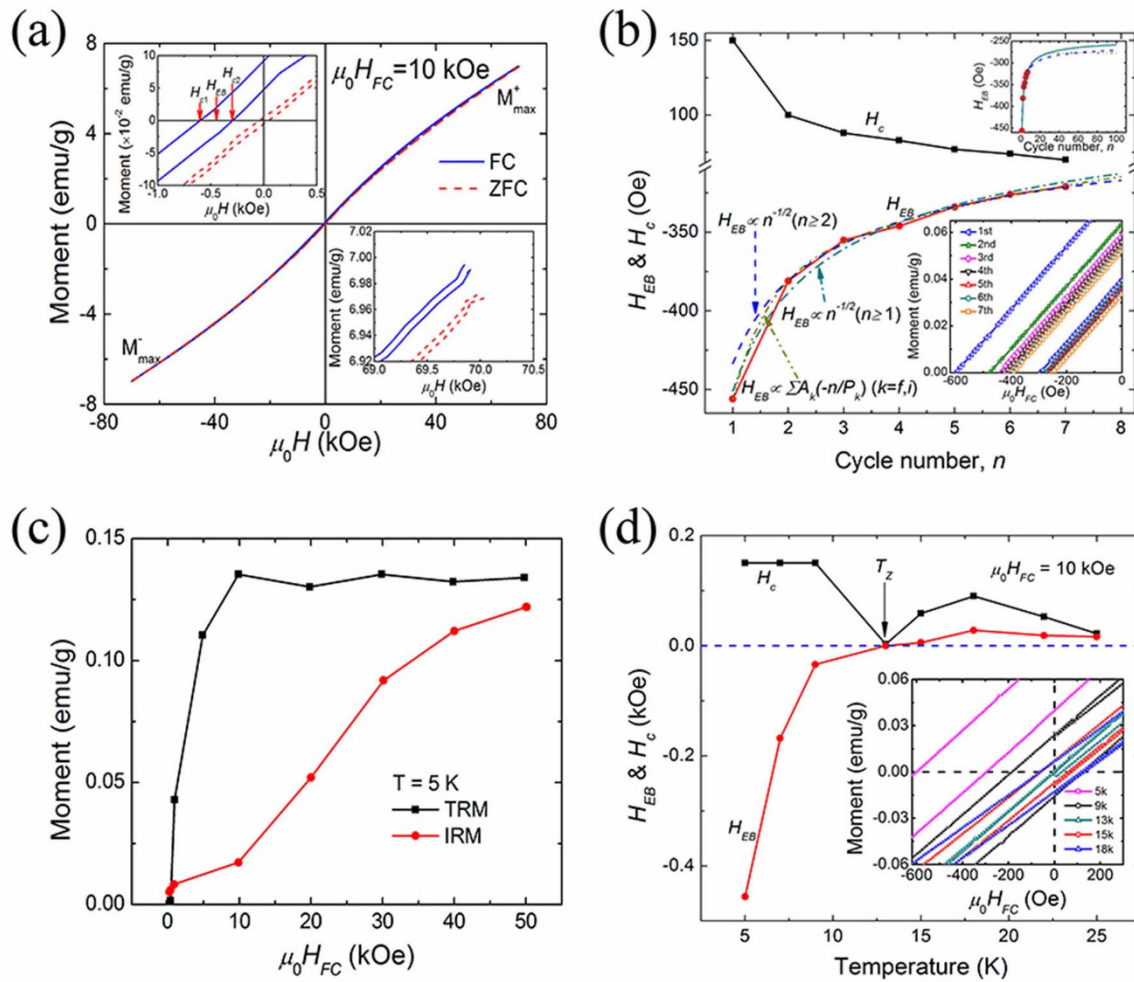
Figure 4 | Exchange bias characterization. (a), The hysteresis loop at 5 K after FC under 10 kOe with obvious exchange bias behavior. Upper inset shows the exchange-bias field H_{EB}, and the left and right coercive fields H_{c1} and H_{c2}. Lower inset shows the open loop due to magnetization relaxation. (b), The H_{EB} and H_c dependence on cycle number (training effect) with different fitting methods. The lower inset shows the $M(H)$ dependence on cycle number, and the upper inset compares H_{EB} after a high number of cycles based on different fitting methods. (c), The thermoremanent magnetization (TRM) and isothermoremanent magnetization (IRM) dependences on applied magnetic fields at 5 K were measured in the field range of 0.4 to 50 kOe. (d), The dependence of H_c and H_{EB} on temperature after cooling in a 10 kOe magnetic field indicates the spin glass behavior. The inset shows the $M(H)$ loops at different temperatures.

(5) is applicable only for $n > 1$. A significant decrease in the H_{EB} takes place between the first and the second hysteresis cycles, suggesting that AFM domains (rearrangements) are present. With each cycle, a spin rearrangement takes place, and this modifies the exchange bias field. It is not possible to describe the curve for H_{EB} dependence on n by only one exponent. The monotonic evolution of H_{EB} as a function of n appears to be due to the interfacial spin rearrangement on the magnetically disordered FM/AFM interface. The interfacial spin frustration can enhance the interface area and keep the total spin number. At the FM/AFM interface, the AFM magnetic anisotropy is assumed to be modified after field cooling, which results in two different types of AFM uncompensated spins: frozen and rotatable AFM uncompensated spins. The two types of spin are rigidly exchange coupled to the AFM and the FM layers, respectively[44]. To estimate the relaxation of the exchange bias as a function of n from $n = 1$, the following expression was adopted:

$$\mu_0 H_{EB} = \mu_0 H_{EB}^e + A_f \exp\left(-n/P_f\right) + A_i \exp\left(-n/P_i\right), \qquad (6)$$

where A_f and P_f are parameters related to the change in the frozen spins, A_i and P_i are evolving parameters of the interfacial magnetic frustration between FM and AFM. The A parameters have the

dimension of magnetic field (Oe), while the P parameters are dimensionless and resemble a relaxation time, where a continuous variable is replaced by a discrete variable, namely, the hysteresis index n. The parameters obtained from the fit to the H_{EB} data are $\mu_0 H_{EB}^e = -276.988$ Oe, $A_f = -382.233$ Oe, $P_f = 0.629$, $A_i = -116.206$ Oe, and $P_i = 7.109$. Eq. (6) fits the experimental data very well, as shown in Figure 4(b). The upper inset of Figure 4(b) shows the extrapolated fitting results to $n = 100$ using Eqs. (5) and (6). It is found that the $\mu_0 H_{EB}^e$ obtained from Eq. (6) is higher than that obtained from Eq. (5), and it is easy to saturate with prolonged cycling. Within the spin-glass approach, an ~10 times sharper contribution due to uncompensated spins at the interface compared with a slower decrease from the frozen uncompensated spins can be distinguished from the total relaxation from Eq. (6).

The training effect can also be explained in terms of the demagnetization of the non-FM surface regions[45]. A relaxation of the surface spin configuration to equilibrium state is induced due to the surface drag of the exchange interaction during the FM domain switches back and forth under the influence of the applied field. This phenomenon is relevant for the spin-glass-like behaviour observed in our sample. The consecutive circulation of applied field cannot drag all the frozen spin-glass-like-spins along with the

cooling field direction. So these spins fall into other metastable configurations and do not contribute to the strength of exchange coupling at the interfaces. Therefore, the observed training effect in MnO_2 can be interpreted well by the spin configurational relaxation model[40].

Spin Glass Behavior. To examine the spin-glass-like behaviour of the α-MnO_2 nanowire shell, the thermoremanent magnetization (TRM) and isothermoremanent magnetization (IRM) dependences on applied magnetic fields at 5 K were measured in the field range of 0.4 to 50 kOe. To measure the TRM, the system was cooled in the specified field from 305 K down to 5 K, the field was removed, and then the magnetization was recorded. To measure the IRM, the sample was cooled in zero field from 305 K down to 5 K, and the field was then momentarily applied, removed again, and the remanent magnetization recorded. Depending on the different cooling and magnetization process, TRM and IRM probe two different magnetization states in the system. The TRM explores the remanent magnetization state in zero field after freezing in a certain magnetization in an applied field during FC. However, the IRM explores the remanent magnetization for a demagnetized system that is magnetized at low temperature. Therefore, the TRM and IRM dependences on magnetic field show a characteristic difference for different systems, such as spin-glass[46], diluted AFM in a magnetic field[47], or core-shell behaviour[39]. The TRM/IRM behaviour in this work is shown in Figure 4(c). Two obvious features are in agreement with the case of a spin-glass system. First, the IRM increases relatively strongly with increasing field and then meets the TRM curve. Second, the TRM exhibits a characteristic peak at intermediate fields and saturates quickly after the peak value, which is also reproduced from several other studies found in the literature[48,49].

In order to confirm the spin glass behaviour, the dependence of H_c and H_{EB} on temperature after cooling in a 10 kOe magnetic field is shown in Figure 4(d). One of the main features is the behaviour of H_c before and after a certain temperature, T_Z, the temperature at which $H_c = 0$. When T < T_Z, the H_c is independent of the temperature. It drops quickly to zero when the temperature approaches T_Z and increases when the T > T_Z, showing a peak value at ∼18 K. It should be noted that the T_Z value is similar to T_N in this system. Another feature is that the negative value of H_{EB} shifts to positive with increasing temperature, which can be observed clearly on the $M(H)$ loops, as shown in the inset of Figure 4(d). These features are the typical spin glass behaviour which can be found in conventional exchange-bias systems[50]. The sign change occurring at T_Z can be seen in Figure 4(d). The effect is markedly different from the inverse exchange bias caused by antiferromagnetic interface coupling[51,52] and by the memory effect[53], because the former can cause a sign change with temperature in a small cooling-field window and, to be realized, the latter requires special field-cooling procedures[54,55]. Ali et al. explain the positive H_{EB} using a random-field model for long-range oscillatory Ruderman–Kittel–Kasuya–Yosida (RKKY) coupled spins[50].

Discussion

The influence of the spin state on the exchange bias behaviour has been noted in the above analysis. Exchange bias behaviour has been observed in nanoparticles composed of materials which are antiferromagnetic for normal bulk samples. The origin of the spin glass behaviour depends greatly on the surface state due to the high specific surface area[56]. However, the precise identification of the nature of the surface contribution has remained unclear. Terms such as "disordered surface state", "loose surface spins", "uncoupled spins", and "spin-glass like behaviour", express the uncertainty in the description of the shell contribution. The mixed valence model was always used to explain ferromagnetic behaviour in an antiferromagnetic matrix, such as the coexistence of Mn^{4+}, Mn^{3+}, and Mn^{2+} [35].

Following the qualitative consideration of Goodenough[57], antiferromagnetic superexchange interaction is expected for the $Mn^{4+}(3d^3)$–O–$Mn^{4+}(3d^3)$ path, and a ferromagnetic superexchange interaction is expected for the $Mn^{3+}(3d^4)$–O–$Mn^{4+}(3d^3)$ and $Mn^{3+}(3d^4)$–O–$Mn^{3+}(3d^4)$ paths. In particular, not only the superexchange interaction, but also a ferromagnetic double-exchange interaction is expected for $Mn^{3+}(3d^4)$–$Mn^{4+}(3d^3)$ pairs. Therefore, ferromagnetic clusters are formed in the antiferromagnetic matrix via ferromagnetic Mn^{3+}–O–Mn^{4+}, Mn^{3+}–O–Mn^{3+}, Mn^{3+}–Mn^{4+}, and Mn^{3+}–Mn^{3+} interactions. Coexistence of ferromagnetic and antiferromagnetic phases has been found in many manganites[58]. Presumably, a similar situation can be imagined in α-MnO_2 nanowires.
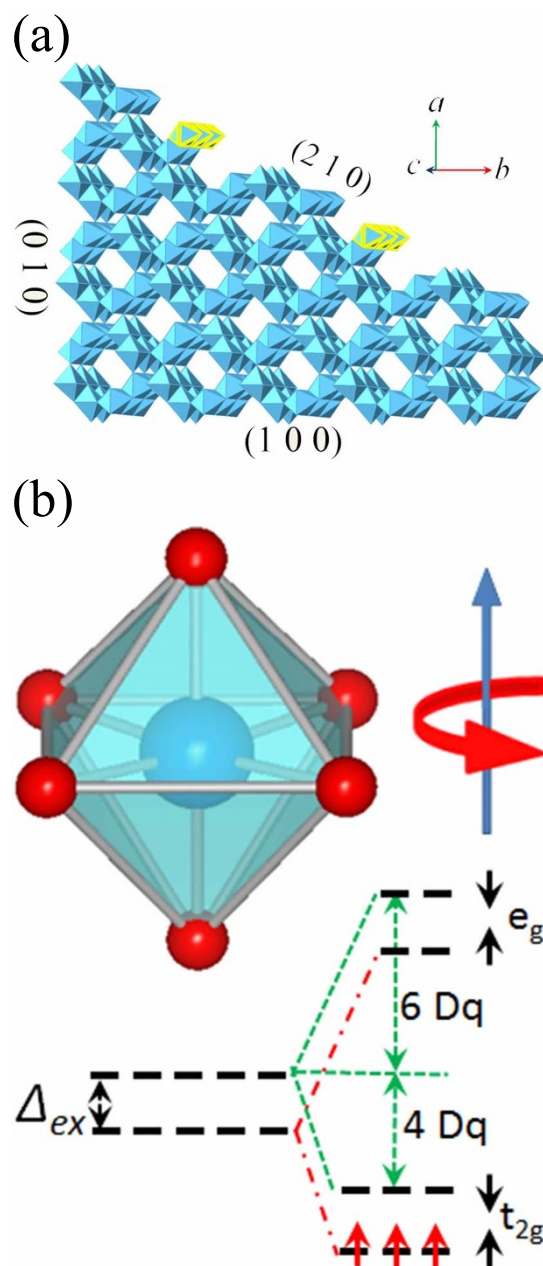

Figure 5 | Origination of magentic moment. (a), Comparison of surface states of (1 0 0), (0 1 0), and (2 1 0) planes in α-MnO_2 nanowires composed of MnO_6 octahedra. The highlighted parts indicate the weak linked MnO_6 octahedral chains on the (2 1 0) plane when it is at the surface. (b), Electron configuration of the Mn 3d levels of Mn^{4+} and the induced magnetic moment in MnO_6 octahedron.

However, both XPS detection and μ_{eff} estimation exclude the possibility of any significant presence of Mn^{3+} and Mn^{2+}. That is to say, the other ions make very weak contributions to the spin glass behavior and the obvious exchange bias effect in α-MnO_2 nanowires, even if they are present in trace levels, judging from the μ_{eff} value of α-MnO_2. The unique magnetism must come from the surface structure induced net magnetic moments. Considering the square tunnel structure of α-MnO_2, the surface state depends greatly on the different planes exposed to the free space. From the microstructural analysis, the surface planes for the nanowires are (2 1 0), rather than (1 0 0) or (0 1 0). The plane structures of the above three planes are compared in Figure 5(a). The (1 0 0) plane is equivalent to (0 1 0), judging from the arrangement of MnO_6 octahedra, and the open tunnels form zigzag surfaces. The (2 1 0) plane forms an irregular step-type surface, which consists of steps and two adjacent grooves. Some MnO_6 octahedral chains are linked with the matrix on one side, as indicated by the highlighted parts in Figure 5(a). This kind of MnO_6 octahedron is also easy to miss on the rough surface of α-MnO_2 nanowires during the crystal growth.

The electron configuration for the Mn^{4+} ($Mn\ 3d^3$) energy level is illustrated in Figure 5(b). The exchange interactions Δ_{ex} splits the Mn $3d$ energy level into spin-up ($\uparrow$) and spin-down ($\downarrow$) states. Each spin state is further split by the octahedral ligand-field splitting parameter 10 Dq into a low energy triply degenerate orbital, labelled as t_{2g}, and a high energy doubly degenerate orbital, labeled as e_g, where 10 Dq is the difference between t_{2g} and e_g orbitals. In an octahedral ligand field, the three t_{2g} orbitals lie 4 Dq below the average energy and the two e_g orbitals lie 6 Dq above the average energy. Therefore, in the Mn $3d^3$ energy level, the three $3d$ electrons occupy $t_{2g}\uparrow$ orbitals as shown in Figure 5(b). Consequently, the Mn^{4+} shows very stable net magnetic moment because there is no spare electron occupying the high energy orbitals to excite high-spin state. The net magnetic moment comes from the uncoupled spins and induces exchange bias behavior during its coupling with the antiferromagnetic matrix, which has never been observed in pure α-MnO_2 with other nanostructures[37,59].

Methods

Sample Preparation. α-MnO_2 rectangular nanowires were synthesized by a hydrothermal method with microwave-assisted procedures at 140°C for 1 h, with Mn^{2+} as the source: $Mn^{2+} + (NH_4)_2S_2O_8 + 2H_2O \rightarrow MnO_2 + (NH_4)_2SO_4 + 2H_2SO_4$. The microwave radiation technique was employed to increase the formation rate, minimize the size, and vary the morphologies of the nanostructures. Moreover, a small amount of H_2SO_4 was added in solution to adjust the pH value of the solution, since the size and morphology of the nanoparticles show a strong dependence on the pH value of the formation environment[60]. In a typical synthesis, $MnCO_3$ (Aldrich, 99.9%), $(NH_4)_2S_2O_8$ (Aldrich, >98%), HNO_3 (>90%), and H_2SO_4 (Aldrich, 95–98%) were used as-received without further purification. 0.02 mol $MnCO_3$ was dissolved in 200 mL deionized water, and 0.04 mol HNO_3 was then added to make a transparent solution. 0.02 mol $(NH_4)_2S_2O_8$ was added, and and the solution was diluted to 300 mL. After the addition was completely dissolved, 20 mL concentrated H_2SO_4 was added, and the solution was diluted to 400 mL and stirred for 30 min. The hydrothermal treatment was performed in a Teflon-lined autoclave, with heating at 140°C for 1 hour in a microwave device. After the reaction was complete, the solution was cooled down to room temperature, and the resulting suspensions were centrifuged in order to separate the precipitate from the mother liquid. The precipitate was washed and centrifuged two times and then dried at 80°C overnight.

Properties Characterization. The sample was microstructurally characterized and analysed by X-ray diffraction (XRD: GBCMMA, Cu K_α, $\lambda = 0.154056$ nm) and Rietveld refinement, X-ray photoelectron spectroscopy (XPS: EscaLab 220-IXL, Al K_α), field emission gun scanning electron microscopy (FEG-SEM: JSM-6700F), and transmission electron microscopy (TEM: JEOL-2010) with high resolution TEM (HRTEM) using 200 kV. Selected area electron diffraction (SAED) patterns were also collected for crystal structure analysis. Magnetic properties were measured using a commercial vibrating sample magnetometer (VSM) model magnetic properties measurement system (MPMS: Quantum Design, 14 T) in applied magnetic fields up to 70 kOe. The nanoparticles were packed into a polypropylene powder holder, which is an injection molded plastic part designed for use as a powder container during the VSM measurement process. The polypropylene powder holder was mounted in a brass trough, which was made from cartridge brass tubing with a cobalt-hardened

gold plated finish. Both the polypropylene powder holder and the brass trough were made by Quantum Design as commercial VSM sample holders with negligible magnetic moments.

1. Heiligtag, F. J. & Niederberger, M. The fascinating world of nanoparticle research. *Mater. Today* **16**, 262–271 (2013).
2. Sun, Z. *et al.* Generalized self-assembly of scalable two-dimensional transition metal oxide nanosheets. *Nat Commun* **5** (2014).
3. Fang, X., Bando, Y., Gautam, U. K., Ye, C. & Golberg, D. Inorganic semiconductor nanostructures and their field-emission applications. *J. Mater. Chem.* **18**, 509–522 (2008).
4. Sun, Z. *et al.* Rational Design of 3D Dendritic TiO_2 Nanostructures with Favorable Architectures. *J. Am. Chem. Soc.* **133**, 19314–19317 (2011).
5. Sun, Z. *et al.* Robust superhydrophobicity of hierarchical ZnO hollow microspheres fabricated by two-step self-assembly. *Nano Research* **6**, 726–735 (2013).
6. Yamauchi, Y. *et al.* Ferromagnetic Mesostructured Alloys: Design of Ordered Mesostructured Alloys with Multicomponent Metals from Lyotropic Liquid Crystals. *Angew. Chem., Int. Ed.* **48**, 7792–7797 (2009).
7. Hu, M. *et al.* Synthesis of Prussian Blue Nanoparticles with a Hollow Interior by Controlled Chemical Etching. *Angew. Chem., Int. Ed.* **51**, 984–988 (2012).
8. Hu, M. *et al.* Sophisticated Crystal Transformation of a Coordination Polymer into Mesoporous Monocrystalline Ti–Fe-Based Oxide with Room-Temperature Ferromagnetic Behavior. *Chemistry – An Asian Journal* **6**, 3195–3199 (2011).
9. Li, W. X., Sun, Z. Q., Tian, D. L., Nevirkovets, I. P. & Dou, S. X. Platinum dendritic nanoparticles with magnetic behavior. *J. Appl. Phys.* **116**, 033911 (2014).
10. Dormann, J. L., Fiorani, D. & Tronc, E. Magnetic relaxation in fine-particle systems. *Adv. Chem. Phys.* **98**, 283–494 (1997).
11. Seto, T. *et al.* Magnetic properties of monodispersed Ni/NiO core-shell nanoparticles. *J. Phys. Chem. B* **109**, 13403–13405 (2005).
12. Barbic, M. & Scherer, A. Magnetic nanostructures as amplifiers of transverse fields in magnetic resonance. *Solid State Nucl. Magn. Reson.* **28**, 91–105 (2005).
13. Jensen, P. J. Magnetic recording medium with improved temporal stability. *Appl. Phys. Lett.* **78**, 2190–2192 (2001).
14. Kohn, A. *et al.* The antiferromagnetic structures of $IrMn_3$ and their influence on exchange-bias. *Scientific Reports* **3**, 7 (2013).
15. Rana, R., Pandey, P., Singh, R. P. & Rana, D. S. Positive exchange-bias and giant vertical hysteretic shift in $La_{0.3}Sr_{0.7}FeO_3/SrRuO_3$ bilayers. *Scientific Reports* **4**, 8 (2014).
16. Moodera, J. S., Nassar, J. & Mathon, G. Spin-tunneling in ferromagnetic junctions. *Annu. Rev. Mater. Sci.* **29**, 381–432 (1999).
17. Batlle, X. & Labarta, A. Finite-size effects in fine particles: Magnetic and transport properties. *J. Phys. D-Appl. Phys.* **35**, R15–R42 (2002).
18. Zheng, X. G. *et al.* Finite-size effect on Neel temperature in antiferromagnetic nanoparticles. *Phys. Rev. B* **72**, 014464 (2005).
19. Neel, L. *Comptes Rendus* **252**, 4075 (1961).
20. Salabas, E. L., Rumplecker, A., Kleitz, F., Radu, F. & Schuth, F. Exchange anisotropy in nanocasted Co_3O_4 nanowires. *Nano Lett.* **6**, 2977–2981 (2006).
21. Winkler, E., Zysler, R. D., Mansilla, M. V. & Fiorani, D. Surface anisotropy effects in NiO nanoparticles. *Phys. Rev. B* **72**, 132409 (2005).
22. Morup, S. & Frandsen, C. Thermoinduced magnetization in nanoparticles of antiferromagnetic materials. *Phys. Rev. Lett.* **92**, 217201 (2004).
23. Kodama, R. H., Makhlouf, S. A. & Berkowitz, A. E. Finite Size Effects in Antiferromagnetic NiO Nanoparticles. *Phys. Rev. Lett.* **79**, 1393 (1997).
24. Tomou, A. *et al.* Weak ferromagnetism and exchange biasing in cobalt oxide nanoparticle systems. *J. Appl. Phys.* **99**, 123915 (2006).
25. Punnoose, A. & Seehra, M. S. Hysteresis anomalies and exchange bias in 6.6 nm CuO nanoparticles. *J. Appl. Phys.* **91**, 7766–7768 (2002).
26. Gazeau, F., Dubois, E., Hennion, M., Perzynski, R. & Raikher, Y. Quasi-elastic neutron scattering on γ-Fe_2O_3 nanoparticles. *Europhys. Lett.* **40**, 575–580 (1997).
27. Parker, F. T., Foster, M. W., Margulies, D. T. & Berkowitz, A. E. Spin canting, surface magnetization, and finite-size effects in γ-Fe_2O_3 particles. *Phys. Rev. B* **47**, 7885 (1993).
28. Fauth, K., Goering, E., Schutz, G. & Kuhn, L. T. Probing composition and interfacial interaction in oxide passivated core-shell iron nanoparticles by combining x-ray absorption and magnetic circular dichroism. *J. Appl. Phys.* **96**, 399–403 (2004).
29. Lin, D., Nunes, A. C., Majkrzak, C. F. & Berkowitz, A. E. Polarized neutron study of the magnetization density distribution within a $CoFe_2O_4$ colloidal particle. 2. *J. Magn. Magn. Mater.* **145**, 343–348 (1995).
30. Lopez-Ortega, A. *et al.* Size-Dependent Passivation Shell and Magnetic Properties in Antiferromagnetic/Ferrimagnetic Core/Shell MnO Nanoparticles. *J. Am. Chem. Soc.* **132**, 9398–9407 (2010).
31. Banerjee, D. & Nesbitt, H. W. XPS study of dissolution of birnessite by humate with constraints on reaction mechanism. *Geochim. Cosmochim. Acta* **65**, 1703–1714 (2001).
32. Mizusaki, S. *et al.* Ferromagnetism in $CaMn_{1-x}Ir_xO_3$. *J. Phys.-Condens. Matter* **20**, 235242 (2008).
33. Gupta, R. P. & Sen, S. K. Calculation of multiplet structure of core p-vacancy levels. *Phys. Rev. B* **10**, 71–77 (1974).

34. Gupta, R. P. & Sen, S. K. Calculation of multiplet structure of core p-vacancy levels. 2. *Phys. Rev. B* **12**, 15–19 (1975).

35. Yamamoto, N., Endo, T., Shimada, M. & Takada, T. Single-crystal growth of α-MnO_2. *Jpn. J. Appl. Phys.* **13**, 723–724 (1974).

36. Zhang, T., Zhou, T. F., Qian, T. & Li, X. G. Particle size effects on interplay between charge ordering and magnetic properties in nanosized $La_{0.25}Ca_{0.75}Mn_3$. *Phys. Rev. B* **76**, 174415 (2007).

37. Yang, J. B., Zhou, X. D., James, W. J., Malik, S. K. & Wang, C. S. Growth and magnetic properties of $MnO_{2-\delta}$ nanowire microspheres. *Appl. Phys. Lett.* **85**, 3160–3162 (2004).

38. Mulyukov, K. Y., Valiev, R. Z., Korznikova, G. F. & Stolyarov, V. V. The Amorphous $Fe_{83}Nd_{13}B_4$ Alloy Crystallization Kinetics and High Coercivity State Formation. *physica status solidi (a)* **112**, 137–143 (1989).

39. Benitez, M. J. *et al.* Evidence for core-shell magnetic behavior in antiferromagnetic Co_3O_4 nanowires. *Phys. Rev. Lett.* **101**, 097206 (2008).

40. Binek, C. Training of the exchange-bias effect: A simple analytic approach. *Phys. Rev. B* **70**, 014421 (2004).

41. Hoffmann, A. Symmetry driven irreversibilities at ferromagnetic-antiferromagnetic interfaces. *Phys. Rev. Lett.* **93**, 097203 (2004).

42. Schlenke, C. & Paccard, D. Couplages ferromagnetiques-antiferromagnetiques: etude des contractions de cycles dhysteresis a laide dun traceur de cycle tres bassess frequences. *J. Phys.* **28**, 611–616 (1967).

43. Gredig, T., Krivorotov, I. N. & Dahlberg, E. D. Magnetization reversal in exchange biased Co/CoO probed with anisotropic magnetoresistance. *J. Appl. Phys.* **91**, 7760–7762 (2002).

44. Radu, F. & Zabel, H. in *Magnetic Heterostructures* Vol. 227 *Springer Tracts in Modern Physics* (eds Hartmut Zabel & SamuelD Bader) Ch. 3, 97–184 (Springer Berlin Heidelberg, 2008).

45. Keller, J. *et al.* Domain state model for exchange bias. II. Experiments. *Phys. Rev. B* **66**, 014431 (2002).

46. Tholence, J. L. & Tournier, R. Susceptibility and remanent magnetization of a spin glass. *J. Phys. Colloq.* **35**, C4(229)–C224(235) (1974).

47. Machado, F. L. A., Montenegro, F. C., Rezende, S. M., Azevedo, L. J. & Clark, W. G. Spin-glass behavior in the Al-Mn quasi-crystalline alloys. *J. Appl. Phys.* **69**, 5150–5150 (1991).

48. Kinzel, W. Remanent magnetization in spin-glasses. *Phys. Rev. B* **19**, 4595 (1979).

49. Binder, K. & Young, A. P. Spin glasses: Experimental facts, theoretical concepts, and open questions. *Rev. Mod. Phys.* **58**, 801 (1986).

50. Ali, M. *et al.* Exchange bias using a spin glass. *Nat. Mater.* **6**, 70–75 (2007).

51. Nogues, J., Lederman, D., Moran, T. J. & Schuller, I. K. Positive exchange bias in FeF_2-Fe bilayers. *Phys. Rev. Lett.* **76**, 4624–4627 (1996).

52. Ohldag, H., Shi, H., Arenholz, E., Stohr, J. & Lederman, D. Parallel versus antiparallel interfacial coupling in exchange biased Co/FeF_2. *Phys. Rev. Lett.* **96**, 027203 (2006).

53. Gokemeijer, N. J., Cai, J. W. & Chien, C. L. Memory effects of exchange coupling in ferromagnet/antiferromagnet bilayers. *Phys. Rev. B* **60**, 3033–3036 (1999).

54. Shi, H. T. *et al.* Temperature-induced sign change of the exchange bias in $Fe_{0.82}Zn_{0.18}F_2$/Co bilayers. *J. Appl. Phys.* **93**, 8600–8602 (2003).

55. Shi, H. T., Liu, Z. Y. & Lederman, D. Exchange bias of polycrystalline Co on single-crystalline $Fe_xZn_{1-x}F_2$ thin films. *Phys. Rev. B* **72**, 224417 (2005).

56. Stamps, R. L. Dynamic Magnetic Properties of Ferroic Films, Multilayers, and Patterned Elements. *Adv. Funct. Mater.* **20**, 2380–2394 (2010).

57. Goodenough, J. B. in *Magnetism and the Chemical Bond* (ed Cotton, F. A.) 168–179 (John Wiley & Sons, New York-London, 1963).

58. Savosta, M. M. *et al.* Coexistence of antiferromagnetism and ferromagnetism in $Ca_{1-x}Pr_xMnO_3$ ($x \leq 0.1$) manganites. *Phys. Rev. B* **62**, 9532–9537 (2000).

59. Umek, P. *et al.* Synthesis of 3D Hierarchical Self-Assembled Microstructures Formed from α-MnO_2 Nanotubes and Their Conducting and Magnetic Properties. *J. Phys. Chem. C* **113**, 14798–14803 (2009).

60. Wang, X. & Li, Y. D. Selected-control hydrothermal synthesis of α- and β-MnO_2 single crystal nanowires. *J. Am. Chem. Soc.* **124**, 2880–2881 (2002).

Acknowledgments

Author contributions

W.X.L. designed the study, with advice from S.X.D. The initial synthesis was performed by W.X.L., R.Z. and D.L.T. obtained the X-ray diffraction data, and microstructural observation and electron diffraction patterns were obtained by W.X.L. and Z.Q.S. Rietveld refinements were initially performed by W.X.L. XPS were measured and analyzed by Z.Q.S. Magnetic susceptibility was measured and analyzed by R.Z. and W.X.L. All authors discussed the results; W.X.L. wrote the manuscript, with discussions mainly with Z.Q.S. and S.X.D.

Additional information